第 49 卷 第 2 期
2022 年 2 月

湖南大学学报（自然科学版）
Journal of Hunan University (Natural Sciences)

Vol. 49 No. 2
February 2022

Open Access Article https://doi.org/10.55463/issn.1674-2974.49.2.6

Mapping Ocean Tidal for the Coast of East Sea Area, Viet Nam, by Using the Numerical Model in Curvilinear Coordinates

Kim Tran Thi[1,2]*, Hong Nguyen Thi Thu[1], Toai Nguyen Cong[1], Long Nguyen Khac Thanh[3,4], Phung Nguyen Ky[5], Bay Nguyen Thi[3,4]

[1] Faculty of Marine Resource Management, Ho Chi Minh City University of Natural Resources and Environment, 236B Le Van Sy Street, Ward 1, Tan Binh District, Ho Chi Minh City, Vietnam

[2] Institute for Environment and Resources, Vietnam National University Ho Chi Minh City, Linh Trung Ward, Thu Duc District, Ho Chi Minh City, Vietnam

[3] Department of Fluid Mechanics, Ho Chi Minh City University of Technology, 268 Ly Thuong Kiet Street, Ward 14, District 10, Ho Chi Minh City, Vietnam

[4] Vietnam National University Ho Chi Minh City, Linh Trung Ward, Thu Duc District, Ho Chi Minh City, Vietnam

[5] People's Committee of Thu Duc City, 168 Truong Van Bang Street, Thanh My Loi Ward, Thu Duc City, Ho Chi Minh City, Vietnam

Abstract: Tides and their effects on coastal and estuarine water levels are among the most well-known phenomena in coastal research. This study aims to map the tidal constituent features in the near-shore East Sea area, for better understanding of the mechanisms that cause the transport of sediments in the area. Furthermore, the study also points to the potential of tidal energy in the area, clean energy that needs to be studied for exploitation. The authors applied the hydraulic model in the curvilinear coordinates to calculate for 4 main tidal constituents in the near-shore, namely K_1, O_1, M_2, and S_2 in the East Sea area, Vietnam. The hydraulic model with two-dimensional orthogonal curvilinear grid has the advantage of increasing the accuracy in the results at the domain boundary, with the applying potential in future small-scale studies in the region. According to this method, the simulation results in areas with complex terrain are better because the velocity field is calculated on a curved grid built by shorelines). The calibration and validation of this model are based on water level data at hydrological stations along the Vietnamese coastline. The result of this model is used to map the harmonic constants and tidal ellipse for four tidal constituents; these help to gain information about the tidal deposition in the East Sea, Viet Nam. The coastal area of Vietnam has potential tidal energy; the largest energy is the tidal constituent O_1, followed by the tidal constituents K_1, M_2, and S_2. Tidal ellipses of the residual tidal constituent K_1 and O_1 are large in the Gulf of Tonkin and the Gulf of Thailand. Meanwhile, residual tidal constituent M_2 and S_2 are large in the southeast of Vietnam coastal. These results are the primary data for future research in the area.

Keywords: East Sea, numerical model, the curvilinear coordinates, tidal current.

使用曲线坐标数值模型绘制越南东海沿岸海洋潮汐图

摘要：潮汐及其对沿海和河口水位的影响是沿海研究中最著名的现象之一。本研究旨在绘制东海近岸地区的潮汐成分特征图，以更好地了解导致该地区沉积物迁移的机制。此外，该研究还指出了该地区潮汐能的潜力，这是需要研究开发的清洁能源。作者应用曲线坐标系的水力模型计算了越南东海海域近岸的 4 个主要潮汐成分，即 K_1、O_1、M_2 和 S_2。具有二维

Received: November 11, 2021 / Revised: December 15, 2021 / Accepted: January 27, 2022 / Published: February 28, 2022

About the authors: Kim Tran Thi, Faculty of Marine Resource Management, Ho Chi Minh City University of Natural Resources and Environment, Ho Chi Minh City, Vietnam; Institute for Environment and Resources, Vietnam National University Ho Chi Minh City, Ho Chi Minh City, Vietnam; Hong Nguyen Thi Thu, Faculty of Marine Resource Management, Ho Chi Minh City University of Natural Resources and Environment, Ho Chi Minh City, Vietnam; Toai Nguyen Cong, Faculty of Marine Resource Management, Ho Chi Minh City University of Natural Resources and Environment, Ho Chi Minh City, Vietnam; Long Nguyen Khac Thanh, Department of Fluid Mechanics, Ho Chi Minh City University of Technology, Ho Chi Minh City, Vietnam;Vietnam National University Ho Chi Minh City, Ho Chi Minh City, Vietnam; Phung Nguyen Ky, People's Committee of Thu Duc City, Ho Chi Minh City, Vietnam;

Bay Nguyen Thi, Department of Fluid Mechanics, Ho Chi Minh City University of Technology, Ho Chi Minh City, Vietnam;Vietnam National University Ho Chi Minh City, Ho Chi Minh City, Vietnam;Corresponding author Kim Tran Thi, ttkim@hcmunre.edu.vn

正交曲线网格的水力模型具有提高域边界结果精度的优势，在该地区未来的小规模研究中具有应用潜力。根据该方法，在复杂地形区域的模拟结果更好，因为速度场是在海岸线构建的弯曲网格上计算的）。该模型的校准和验证基于越南海岸线水文站的水位数据。该模型的结果用于绘制四种潮汐成分的调和常数和潮汐椭圆；这些有助于获得有关越南东海潮汐沉积的信息。越南沿海地区具有潜在的潮汐能；最大的能量是潮汐成分 O_1，其次是潮汐成分 K_1、M_2 和 S_2。残余潮汐成分 K_1 和 O_1 的潮汐椭圆在东京湾和泰国湾较大。同时，越南沿海东南部残留潮汐成分 M2 和 S2 较大。这些结果是该领域未来研究的主要数据。

关键词：东海，数值模型，曲线坐标，潮流。

1. Introduction

Tides, rising and falling sea levels worldwide, are one of the most important types of ocean water movements. Tides are the long-period waves that form under the influence of the tidal forces of the Moon and the Sun. Variations in the water level of shallow water of shelves and estuaries are strongly related to the evolution of tides. Study on tidal current dynamics plays a role as important, since, assess coastal flow direction to serve the development calculates the delta estuary.

Tidal analysis and prediction have for long been an important issue for different applications such as safe navigation, hydrographic surveys, and renewable energy [1, 2]. Because the tide is a periodic phenomenon, it can be modeled by a series of periodic functions as sinusoidal ones [3, 4]. For more detailed analyses about the tidal current mechanism, many methods can be used, such as fully analytical models [5, 6], semi-analytical [7, 8], and full numerical simulations [6, 9].

For many cases, using numerical allows simulating tidal current in near-shore under the influence of the bottom morphology [10, 11]. Moreover, tidal current frequencies and amplitudes can be analyzed and predicted using the same mathematical techniques as tidal heights [12]. Yousefi & Veron mentioned that capturing the fluid flow structure is practical to express the governing equations of motion in general orthogonal or non-orthogonal coordinates [13]. It assumes transforming the coordinate system but not the dependent flow variables such as velocity components. The rectangular flow field is interpreted in a curvilinear coordinate system [13].

The advantage of this technique is that the governing equations are significantly more straightforward in the orthogonal coordinate systems and preserve much of the analytical simplicity of their counterpart equations in the Cartesian coordinates. Importantly, the bottom friction coefficient and Coriolis parameter in the setting up model were constants because the Strait of Messina is a small area. A numerical model of tides in the Black Sea and the adjacent Sea of Azov was calibrated with 28 tide gauge observations by Medvedev et al. [14]. Medvedev's study used the 2D version of the Princeton Ocean Model (POM). In the model, the bottom friction force in the momentum equations was determined by the speed of the bottom flow and the friction coefficient (C_b max = 0.0025) for near shore. The coefficient was calculated based on the von Karman constant ($\kappa = 0.4$) and the bed roughness length (z_0= 0.01 m).

In the South China Sea, studies on the near-shore tidal characteristics are quite limited [15-17]. According to Ding [17], the four largest tidal components (O_1, K_1, M_2, and S_2) give a relatively complete picture of the tidal pattern of the Pacific Ocean and the South China Sea and are sufficient for a general description [18].

The co-tidal and co-range charts (tidal phases and amplitudes of the main tidal constituents) proposed by various researchers revealed large uncertainties over the shelf areas. Research using the 2D numerical model simulation detected the M_2 at the shallow part of the Gulf of Thailand [19], Gao et al. simulated the principal tidal constituents M_2, S_2, K_1, and O_1 in the Guangxi Gulf of Tonkin [20].

Wei et al. [21] have mentioned that semi-diurnal tides originate from both the Pacific and Indian oceans, whereas the diurnal tides are mainly from the Pacific Ocean. The mentioned researches showed that the amplitude and phase of tidal constituents M_2, S_2, K_1, and O_1 in the South China Sea, Gulf of Tonkin, and the Gulf of Thailand was constructed with high reliability; however, under bottom friction in near-shore, these characteristics still needed to verify based on the oceanographic station in these areas.

In this study, the objective of this study is to identify the harmonic constants of 4 main tidal constituents (the main semi-diurnal (M_2 and S_2) and diurnal (O_1 and K_1) constituents) in the East Sea, Vietnam.

The hydraulic model with the two-dimensional orthogonal curvilinear grid can increase the accuracy of the results at the domain boundary. This result of the harmonic constants and tidal ellipse key pieces of information to (1) Identify tidal energy research in the near-shore where the friction bed coefficients for four tidal constituents are set up changing the water depth, (2) Mapping harmonic constant of K_1, O_1, M_2 and S_2 tidal constituents in the near-shore East Sea area, Vietnam, (3) Mapping tidal ellipse which serve our understanding of the mechanisms that cause the transport of sediments.

2. Materials and Methods

2.1. Material

The study area is the coastal area at the East Sea, Vietnam, from 99.174 to 112.641 East longitude and 4.528 to 21.772 North latitude. The domain consists of three boundaries: a liquid boundary (Boundary 1) is the East Sea boundaries; the two solid boundaries are the coastline of Vietnam (Boundary 2 and 3) (Fig. 1).

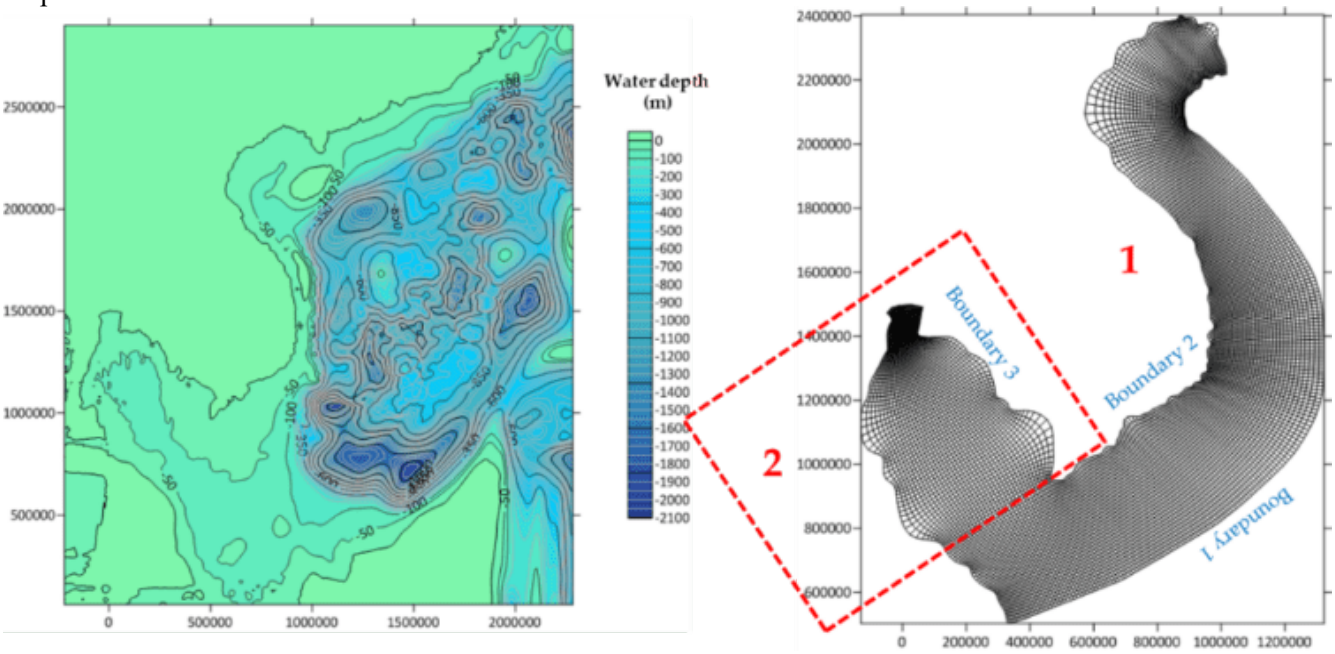

Fig.1 Topography

Input parameters used for the hydraulic model applied to the study area for the main semi-diurnal (M_2 and S_2), and diurnal (O_1 and K_1) constituents are shown in Table 1. The friction bed coefficients for four tidal constituents were set up, changing the water depth with the range of 0.026 to 0.058 while Coriolis parameters changed based on latitude (the Gulf of Thailand (6.73 - 13.46) and the East Sea (4.54 - 21.71)).

Table 1 The parameters in the model

STT	Parameters	K1	O1	M2	S2
1	Time step (dt)	180 s			
2	Sigma	7.26 x 10-5	6.76 x 10-5	14.05 x 10-5	14.54 x 10-5
3	Tidal constituent period	86146 s	92950 s	44714 s	43200 s
4	The density of seawater	kg/m3			

2.2. Boundary Conditions

The constant harmonic data for the three tidal constituents were extracted from the DTU10 Global Tide Model (MIKE21 Global Tide Model) as input data for the three open boundaries at sea.

2.3. Model Verification Data

The parameters of the model were calibrated based on the harmonic constants of 27 tidal stations along the coasts and on islands which are taken from the archives of the Institute of Oceanology, Chinese Academy of Sciences, from the British Admiralty Tide and Tidal Stream Tables (based on at least one-year observation). The harmonic constants at some stations (Kamau, Tammassu, Chandaburi, Satahib Bay, and Songkhla) are obtained from the analysis using the Admiralty Method [22]. The position of these stations is indicated in Fig. 2.

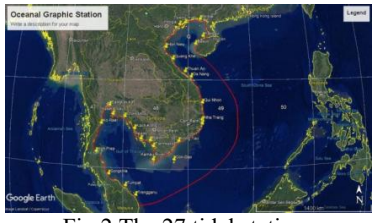

Fig.2 The 27 tidal stations

2.4. The Governing Equations in Cartesian Coordinates

The method of the model derives from the solution of the Reynolds system of equations averaged over the

depth in the curvilinear coordinate systems. The Reynolds equations integrated with depth (1):

$$\begin{aligned}
&\frac{\partial u}{\partial t}+u\frac{\partial u}{\partial x}+v\frac{\partial u}{\partial y}-fv=-g\frac{\partial(\zeta)}{\partial x}-\frac{ku\left(u^2+v^2\right)^{\frac{1}{2}}}{h+\zeta}\\
&\frac{\partial v}{\partial t}+u\frac{\partial v}{\partial x}+v\frac{\partial v}{\partial y}+fu=-g\frac{\partial(\zeta)}{\partial y}-\frac{kv\left(u^2+v^2\right)^{\frac{1}{2}}}{h+\zeta}\\
&\frac{\partial\zeta}{\partial t}+\frac{\partial}{\partial x}[(h+\zeta)u]+\frac{\partial}{\partial y}[(h+\zeta)v]=0
\end{aligned} \quad (1)$$

where u,v - are the velocity components in the x and y direction in Cartesian coordinates; h - total water depth; ζ - the fluctuation of the water surface; t – time; k - Friction bed coefficient; f - the Coriolis parameter.

2.5. The Governing Equations in the Curvilinear Coordinate System

In the curvilinear coordinates (ξ ,η), after some transformations, the equations (1) become the following equations (2).

$$\begin{cases}
p_\tau+gHJ^{-1}\left(g_{22}\varsigma_\xi-g_{12}\varsigma_\eta\right)=\Psi_1\\
q_\tau+gHJ^{-1}\left(g_{11}\varsigma_\eta-g_{12}\varsigma_\xi\right)=\Psi_2\\
JH_\tau+p_\xi+q_\eta=0
\end{cases} \quad (2)$$

Where τ = t; p = JUH; q = JVH; H = h +ζ U,V - The "contravariant" base vectors of the curvilinear coordinate system.

$$U=J^{-1}\left(uy_\eta-vx_\eta\right);V=J^{-1}\left(-vy_\xi-vx_\xi\right) \quad (3)$$

$$\Psi_1=\Psi_{a1}+\Psi_{t1}+\Psi_{k1};\Psi_2=\Psi_{a2}+\Psi_{t2}+\Psi_{k2} \quad (4)$$

Ψa_1 ,Ψa_2 - The nonlinear component in curvilinear coordinate system ξ ,η

Ψt_1,Ψt_2 - Friction bed coefficient; Ψk_1, Ψk_2 - The Coriolis parameter.

$$\Psi_{a1}=-\left[(pU)_\xi+(pV)_\eta+JH\left(U^2\Gamma_{11}^1+2UV\Gamma_{12}^1+V^2\Gamma_{22}^1\right)\right] \quad (5)$$

$$\Psi_{a2}=-\left[(qU)_\xi+(qV)_\eta+JH\left(U^2\Gamma_{11}^2+2UV\Gamma_{12}^2+V^2\Gamma_{22}^2\right)\right] \quad (6)$$

$$\Psi_{t1}=-\frac{K}{H}|v|p \quad (7)$$

$$\Psi_{t2}=-\frac{K}{H}|v|q \quad (8)$$

$\Gamma_{i,j}^k$ - Christoffel symbol type – II ;

e_1, e_2 – the base vectors of the curvilinear coordinate system ξ ,η ;

e^1,e^2 - the "covariant" base vectors $\vec{\mathbf{e}}$

The solution scheme is the C-Arakov Scheme with the alternating direction implicit technique. This scheme can be solved with a time step significantly longer than that determined by the Courant-Freidrichs-Lewy condition.

2.5.1. Mesh Generation

The equation systems used to construct the mesh are elliptic equations – Poisson equations (9).

$$\Delta^2\xi=P(\xi,\eta);\qquad \Delta^2\eta=Q(\xi,\eta) \quad (9)$$

where P and Q are the control functions. The solution of this equation system in the domain (ξ ,η) is:

$$L(r)=g_{22}r_{\xi\xi}-2g_{12}r_{\xi\eta}-g_{11}r_{\eta\eta}=-J^2\left(\mathrm{Pr}_\xi+Qr_\eta\right) \quad (10)$$

J: the "Jacobian" of the transformation:

$$\begin{aligned}
&J=x_\xi x_\eta+y_\xi y_\eta;0\neq J<\infty\\
&r=xi+yj;\\
&g_{22}=x_\eta^2+y_\eta^2=\left|r_\eta\right|^2;\\
&g_{12}=x_\xi x_\eta+y_\xi y_\eta=r_\xi r_\eta;\\
&g_{11}=x_\xi^2+y_\xi^2=\left|r_\xi\right|^2
\end{aligned} \quad (11)$$

The momentum and continuity equations will be solved on this grid after converting to the curvilinear coordinate system. A computational mesh (Fig. 3a) is a mixed curved perpendicular to the computational mesh (the Gulf of Thailand and the East Sea, Vietnam with the size of (90×38) and (34×260) cells with dx, dy in the range of 5000 meters to 11000 meters, respectively). When simulating in the model, the mesh will be solved in L-shape as Fig. 3b.

2.5.2. Boundary Conditions

The boundary conditions at the fluid boundaries give the form of oscillation ζ of each tidal constituent: ζ =A cos(σ t - g), where A, σ , g0: Amplitude, frequency, and phase of the tidal oscillation.

The boundary conditions at the solid boundaries: p=0 on ξ = const; q=0 on η = const.

2.5.3. Energy Balance Equation

Apart from verification by comparing simulation and observation in the harmonic constants of 27 tidal stations along the coasts and islands, the model verification is also implemented based on the equilibrium of the tidal currents of energy. The components of the energy balance equation in the curvilinear coordinate system are:

$$K=\frac{1}{2}\rho\iint_{\Omega^*}J^{-1}H^{-1}\mathrm{p}^2d\Omega^*;P=\frac{1}{2}\rho g\iint_{\Omega^*}J\varsigma^2d\Omega^* \quad (12)$$

$$W=\rho\int_{\eta_0}q\left(\frac{J^{-2}H^{-2}\mathrm{p}^2}{2}+g\varsigma\right)d\varsigma; \quad (13)$$

$$D_1=-K\rho\iint_{\Omega^*}J^{-2}H^{-3}\mathrm{p}^3d\Omega^*;D_2=\frac{2}{dt}\iint_{\Omega^*}\gamma\left(P^*\Delta^2p+Q^*\Delta^2q\right) \quad (14)$$

where:

$$p = JH|v| = \left(g_{11}p^2 + 2g_{12}pq + g_{22}q^2\right)^{1/2}; \quad (15)$$

K- Kinetic Energy; P - Potential energy; W - Energy flows across the liquid boundary;

D1 - Energy dissipation due to bottom friction;

D2 - Energy dissipation when smoothing in the calculation.

P*,Q*: "covariant" component of the velocity vector.

$$P^* = g_{11}U + g_{12}V; Q^* = g_{21}U + g_{22}V \quad (16)$$

The energy balance equation is:

$$\begin{aligned} E_t &= W + D \\ E &= K + P \\ D &= D_1 + D_2 \end{aligned} \quad (17)$$

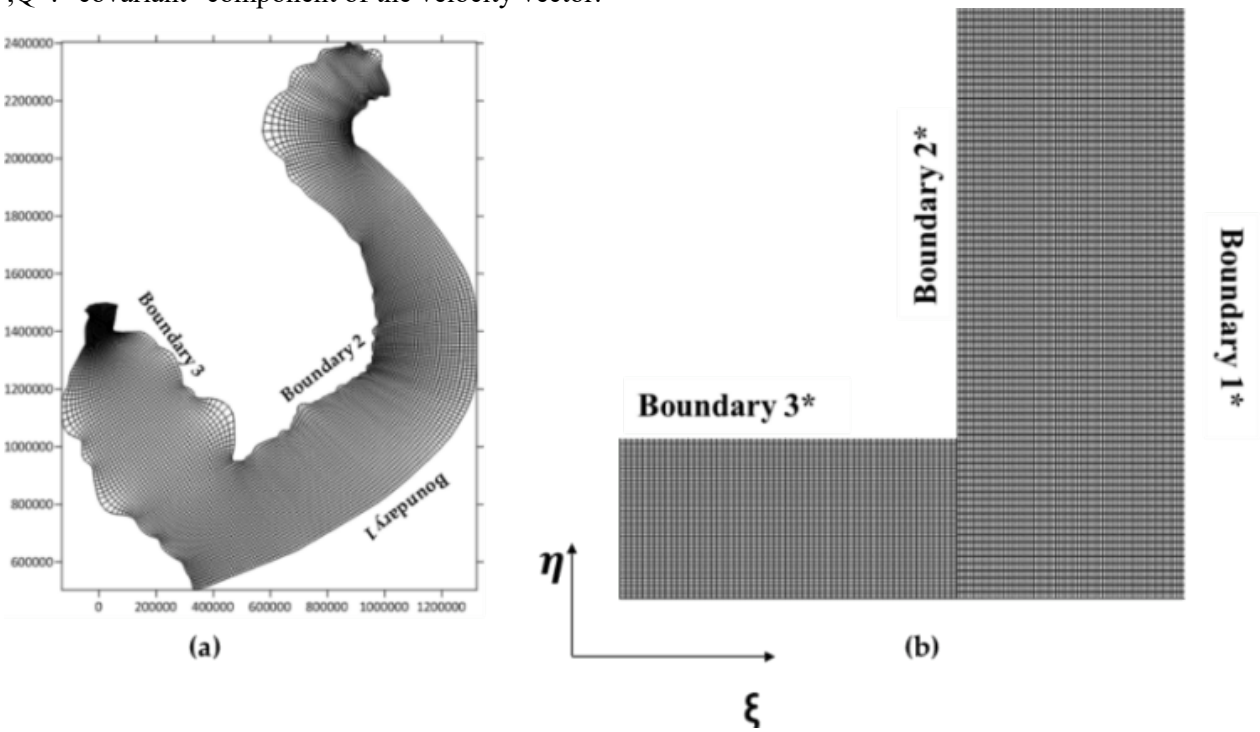

Fig.3 Computation mesh

2.5.4. Analysis of the Hydrodynamic Model in Curvilinear Coordinates to Solve a Problem in U-Channel

The hydrodynamic model is applied to the flat bottom curved channel with a width of 10 m, a length of 90 m, and a rotation angle of 180 degrees with a radius r = 15 m. The spatial step range from 0.5 m to 1.5 m.

The obtained results are shown in Fig. 4 through 13 cross-sections. The results are compared with the experimental results of Shukry [23] and the calculated results in the U-channel when using the hydrodynamic model on the Cartesian coordinate system [24].

Initial conditions: When the water surface is completely still, u, v, ζ at all points are equal to 0.

Boundary conditions: at the lower inlet of the channel, the water level is assumed to be constant over time and equal to 0.25 m; at the upper outlet, time is constant and equal to 0 m.

The calculation results show that the velocity field, in the case when calculated by the hydrodynamic model in curvilinear coordinates (Fig. 4a), is coherent with the results obtained from Shukry's experiment [23] (Fig. 4b).

After the flow passes through the bend of the canal, the velocity field is forced towards the concave bank (Fig. 4a), which is also the main cause of erosion in the curved river sections area in the natural.

When using the hydrodynamic model in the Cartesian coordinate system (Fig. 4c), the results of the velocity field in this area are not optimal when compared with the results in a curvilinear coordinate system; after passing through the bend area, the flow velocity on the concave side is small, almost approaching 0.

3. Results

3.1. The Model Verification of Tidal Constituents K_1, O_1, M_2 and S_2

Validation consists of systematic variation of model parameters and comparison of model simulations. During calibration, comparing measurements and model results improves the model solution for optimal results. The comparison between simulation and observation of the harmonic constants for four constituents of 27 tidal stations along the coasts and on islands is described in Table 2. The model verification results of tidal constituents K_1, O_1, M_2, and S_2 show that the simulation of the study is very close to shown

in [22]. Generally, the phase-lags simulation is later than shown in [22] at most stations. For the M_2 constituent, the simulation results at the 27 stations are lower than those of observation data. In more details, the amplitude simulation at Kamau River, Tammassu, Ha Tien, Ream get the value of 0.5, 0.523, 0.52, 0.3 respectively, compared to 0.15, 0.11, 0.1, 0.07 with observation data (Table 2). Averaged amplitude error between simulation and observation for M_2 constituent is 12.98%, while the phase value is 8.4% (Table 2). Similarly, the averaged amplitude errors between simulation and observation for O_1 and K_1 constituents are 4.8% and 0.48%, respectively. The phase results of these constituents show a good agreement, at 6.87% (O_1 constituent) and 3.5% (K_1 constituent). However, the errors of both amplitude and phase of S_2 constituents are quite larger. The amplitude error is 19%, and that of phase is 17%.

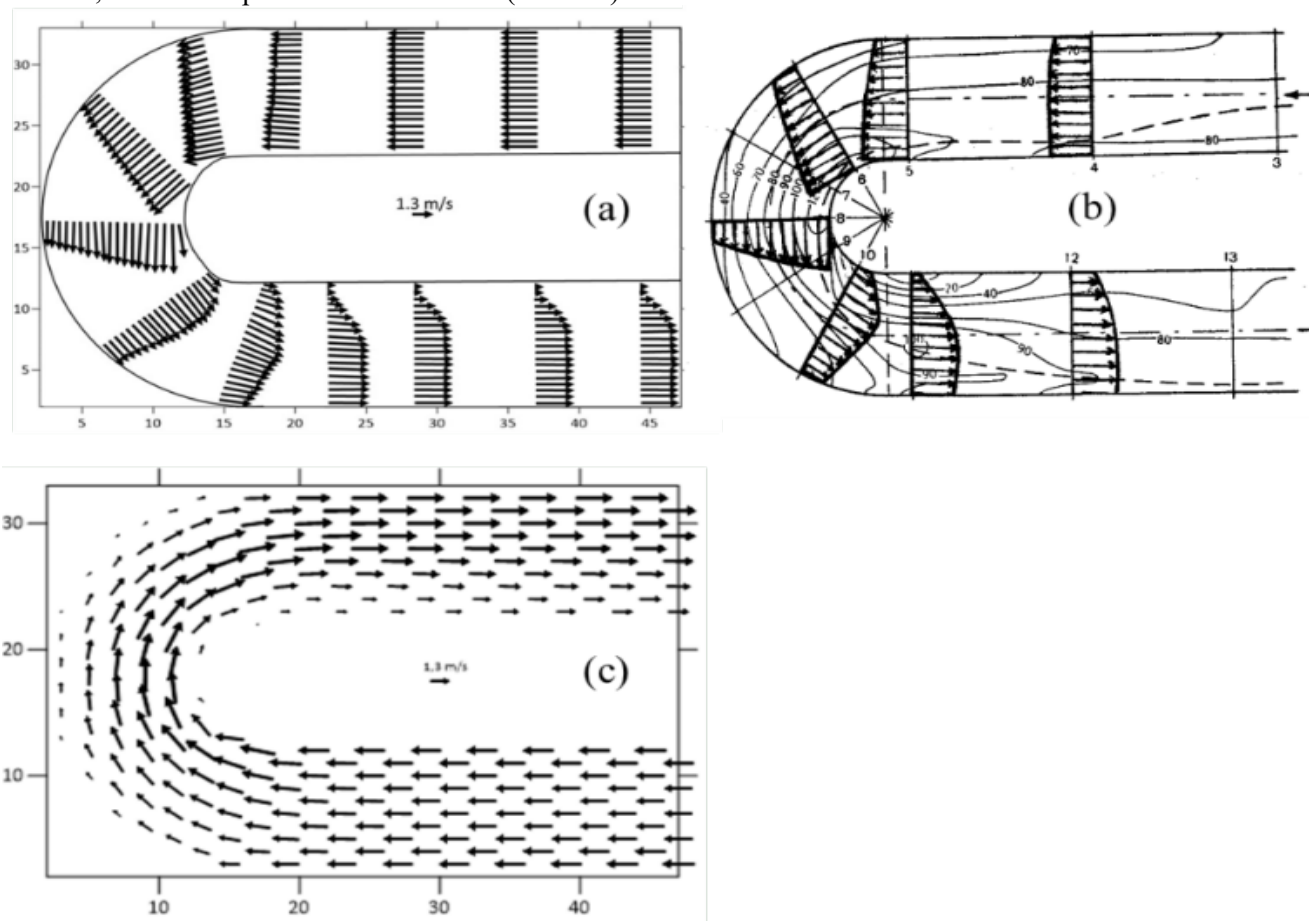

Fig.4 Calculation results in the U-channel by hydrodynamic model on curvilinear coordinates (a), Shukry's experiment [23] (b), and calculation results in U-channel using the model hydrodynamics on the Cartesian coordinate system (c) [24]

3.2. The Energy of Tidal Constituents K_1, O_1, M_2 and S_2

The results show that the energy oscillation in four tidal constituents is stable and sinusoidal. Under the influence of the initial condition, the first periods fluctuate unstably. For better accuracy, the results are extracted from the 5th period onwards. In the Gulf of Tonkin (Fig. 5), the largest total energy (the total of kinetic and potential energies) is the tidal constituent O_1 (20×10^{10}KJ), followed by the tidal constituents K_1 (19×10^{10}KJ), tidal constituent M_2 (3.95×10^{10}KJ), and tidal constituent S_2 (0.495×10^{10}KJ). The kinetic energy of O_1, M_2, and S_2 tidal constituents are noticeably larger than the potential energy, at 19×10^{10}KJ, 3.5×10^{10}KJ, and 0.44×10^{10}KJ, respectively. Meanwhile, the potential energy of the tidal constituent K_1 gets the highest point, at 18.1×10^{10}KJ, followed by the tidal constituents O_1 (16.5×10^{10}KJ), M_2 (3.5×10^{10}KJ), and S_2 (0.41×10^{10}KJ). In the Gulf of Thailand (Fig. 6), the tidal constituents' values are similar to those of Tonkin. The total kinetic and potential energies of O_1 is 17×10^{10}KJ, followed by the tidal constituent K_1 (14×1010KJ), the tidal constituent M_2 (3.25×1010KJ), the tidal constituent S_2 (1.68×1010KJ). The tendencies of kinetic and potential energies are similar. The values of kinetic and potential energies in the Gulf of Thailand are lower significant than these of the Gulf of Tonkin (3 – 4.10^{10}KJ with the tidal constituents K_1 and tidal constituent O_1).

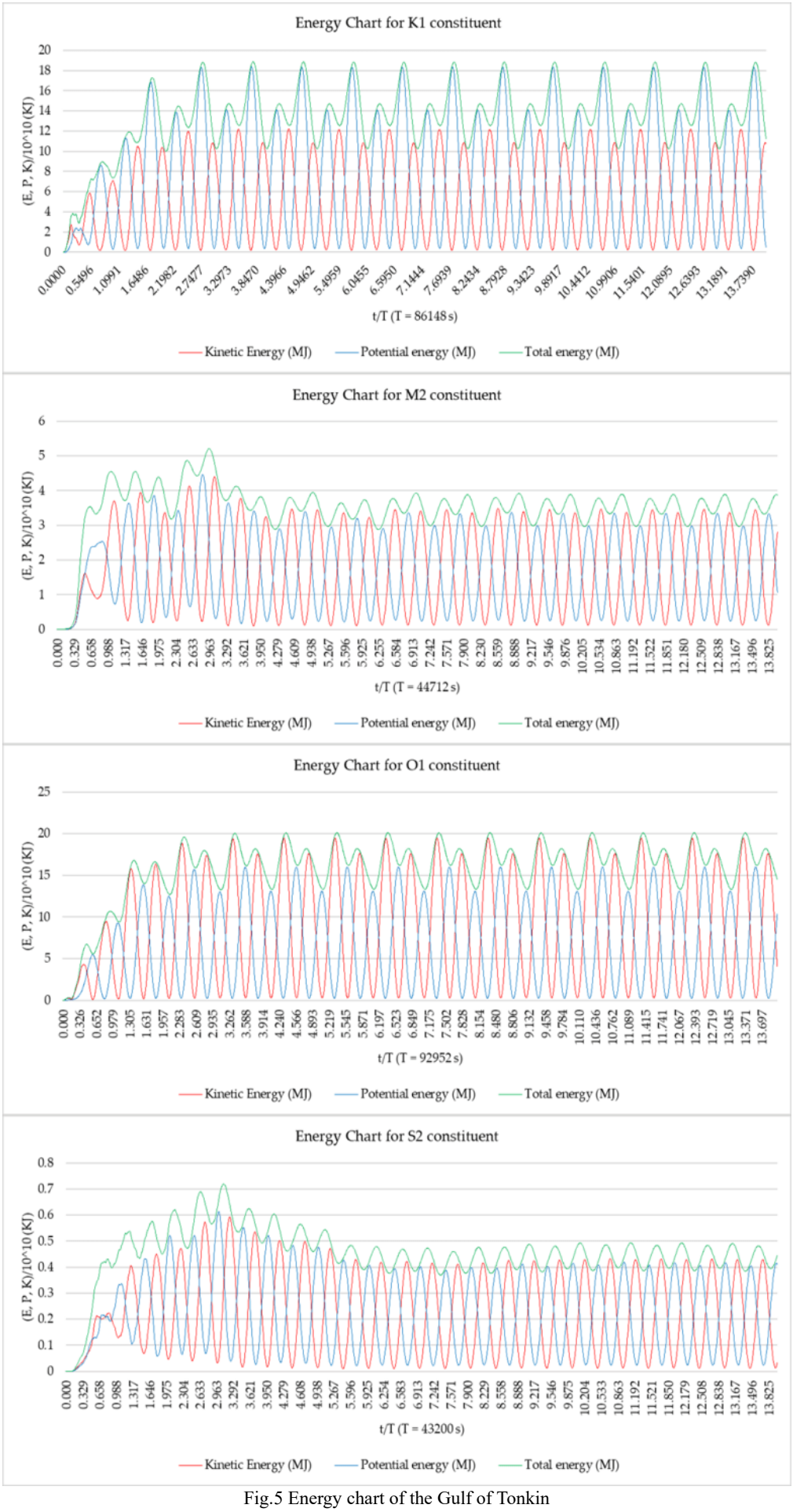

Fig.5 Energy chart of the Gulf of Tonkin

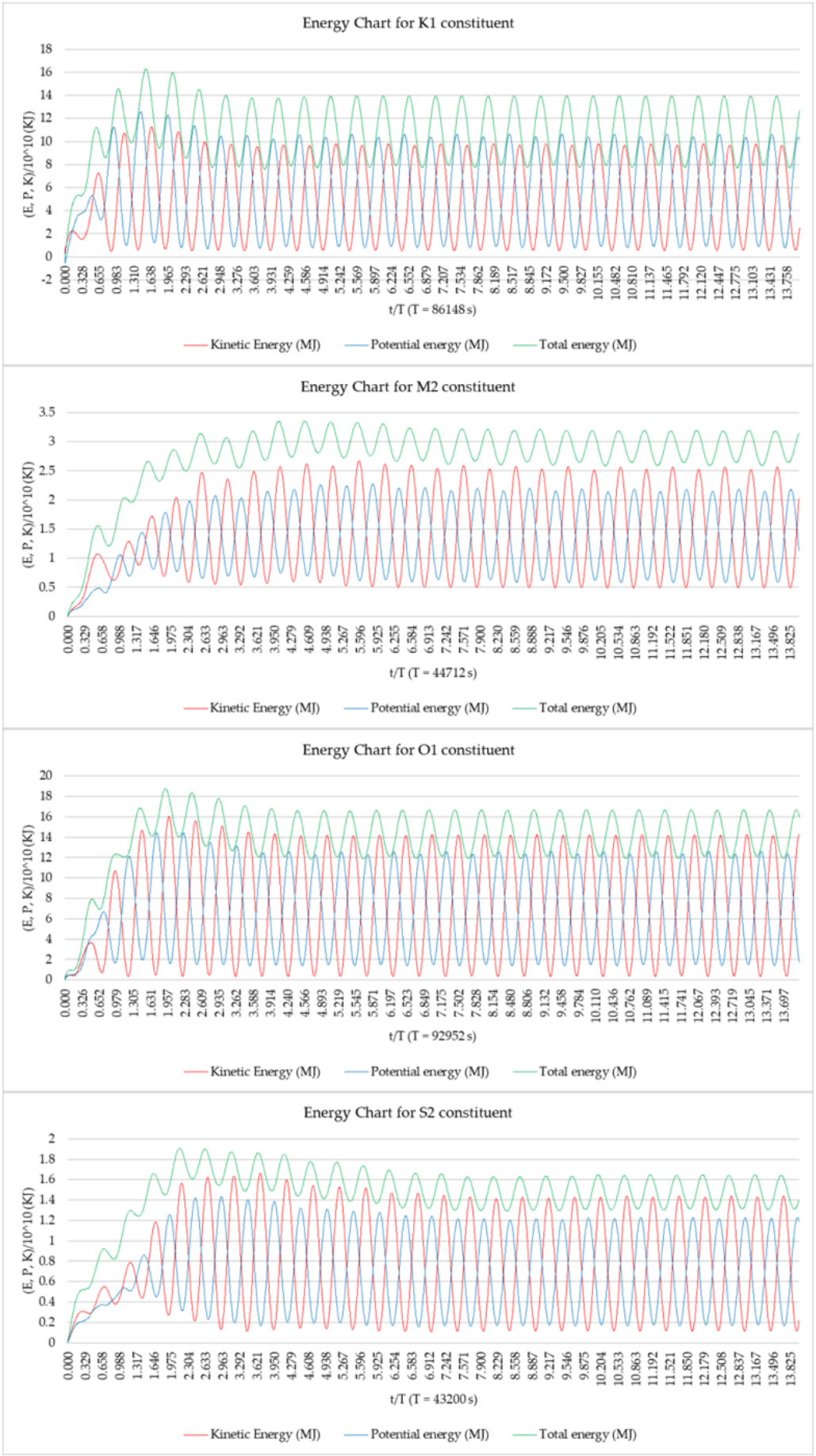

Fig.6 Energy chart of the Gulf of Thailand

Table 2 Comparison between simulation and observation of the harmonic constants for four constituents

No	Place	X	Y	M_2				S_2				O_1				K_1			
				Sim.		Obs.		Sim.		Obs.		Sim.		Obs.		Sim.		Obs.	
				H(m)	g(^{0})	H(m)	g (^{0})	H(m)	g (^{0})	H(m)	g (^{0})	H(m)	g (^{0})	H(m)	g (^{0})	H (m)	g (^{0})	H(m)	g (^{0})
1	Basuo	249247.4	2113599.5	0.198	60	0.18	61	0.031	120	0.06	118	0.7	15	0.62	11	0.6	85	0.54	356
2	Yangpu	325456.1	2193899.6	0.221	140	0.24	150	0.058	160	0.09	204	0.98	25	0.81	18	0.85	120	0.73	10
3	Beihai	301424.1	2376857.7	0.29	190	0.44	177	0.084	200	0.11	237	0.85	50	0.96	34	0.9	140	0.88	19
4	Tsieng mum	771775.2	2339142.6	0.19	185	0.18	179	0.045	220	0.06	230	0.85	42	0.82	30	0.81	128	0.73	22
5	Hongai	714892.5	2318000.1	0.114	160	0.06	144	0.027	190	0.03	147	0.84	42	0.88	48	0.8	125	0.85	25
6	Hon Nieu	580789.4	2078872.3	0.11	32	0.3	31	0.046	20	0.09	113	0.55	50	0.58	57	0.45	120	0.49	31
7	Quang Khe	655539.5	1957600.5	0.13	30	0.18	41	0.048	0	0.05	91	0.37	35	0.27	53	0.3	100	0.21	28
8	Thuan An	781020.1	1833460.8	0.173	340	0.18	351	0.049	50	0.04	58	0.18	300	0.02	19	0.18	10	0.3	1
9	Da Nang	198662.1	1780206.4	0.175	350	0.17	330	0.049	5	0.06	10	0.15	310	0.13	258	0.2	0	0.2	257
10	Qui Nhon	631538.4	1520409.8	0.165	340	0.18	321	0.063	7	0.06	7	0.05	250	0.27	268	0.25	320	0.34	258
11	Nha Trang	304169.7	1349319.6	0.155	325	0.18	321	0.066	20	0.06	351	0.2	240	0.3	258	0.29	330	0.34	254
12	Cam Ranh	303940.0	1314287.2	0.152	320	0.18	329	0.068	25	0.09	15	0.2	240	0.3	265	0.29	330	0.34	254
13	Vung Tau	726308.9	1142999.7	0.83	45	0.79	63	0.32	80	0.3	111	0.35	257	0.46	277	0.4	234	0.61	268
14	Con Dao	679710.8	958386.1	0.7	50	0.79	81	0.32	110	0.27	142	0.27	275	0.46	288	0.42	350	0.64	288
15	Kamau River	472495.5	956166.5	0.5	70	0.15	97	0.15	240	0.06	50	0.22	320	0.21	329	0.4	20	0.37	34
16	Tammassu	472587.1	1086995.5	0.523	200	0.11	135	0.3	40	0.06	00	0.25	20	0.15	14	0.42	80	0.28	25
17	Hatien	441614.9	1146001.8	0.52	280	0.1	190	0.2	45	0.02	353	0.25	60	0.13	52	0.42	100	0.26	45
18	Ream	346792.3	1161036.2	0.3	250	0.07	129	0.18	55	0.07	78	0.22	70	0.14	92	0.4	120	0.22	88
19	Kaoh Kong I	281783.8	1262805.2	0.152	75	0.12	51	0.1	62	0.06	123	0.27	85	0.27	131	0.45	154	0.37	109
20	Chandaburi	181112.6	1379920.8	0.15	130	0.15	125	0.05	140	0.06	312	0.29	110	0.46	129	0.53	160	0.58	125
21	Satahib bay	708168.7	1399193.8	0.2	180	0.24	159	0.1	220	0.09	267	0.37	120	0.46	129	0.6	175	0.64	133
22	Bangkok bar	671391.9	1489295.2	0.408	200	0.55	170	0.34	250	0.27	242	0.42	125	0.46	131	0.65	185	0.67	137
23	Ko Raet	588969.4	1304567.9	0.12	270	0.06	168	0.08	220	0	242	0.33	135	0.34	132	0.57	189	0.52	136
24	Koh Prap	542108.6	1018828.9	0.092	350	0.18	358	0.1	40	0.12	86	0.21	150	0.3	144	0.41	195	0.46	145
25	Songkhla	676661.2	798010.6	0.18	320	0.23	321	0.042	240	0.03	85	0.05	340	0.04	212	0.05	360	0.06	301
26	Tumpat	186427.1	686150.9	0.285	290	0.18	261	0.05	270	0.08	293	0.18	320	0.17	316	0.5	10	0.28	324
27	Trengganu	293149.4	591667.2	0.391	260	0.27	243	0.55	320	0.12	289	0.24	320	0.3	315	0.35	5	0.52	326

The oscillation of the total energy (W – Green line) and loss of energy caused by bottom friction (D_1 – Blue line) has an opposite phase while the total energy oscillates in phase with variation in energy in the domain (E_t – Dark blue line). The energy balance oscillation in the variable region ((W + D – E_t) – Red dash-line) around axis '0' represents the energy balance in the region. The homogeneity of the oscillation of the energy inflow in the region and the energy variation is substantial for all four constituents, and the energy loss because friction (D_2) is virtually small. Fig. 7 illustrates the Balance energy chart of the Gulf of Tonkin (a) and the Gulf of Thailand (b) for the M_2 constituent. The energy balance oscillation in the variable region ((W + D – E_t) – Red dash-line) around axis '0' from the 5th period onwards while the previous periods have values without harmonic oscillation due to the influence of the initial conditions.

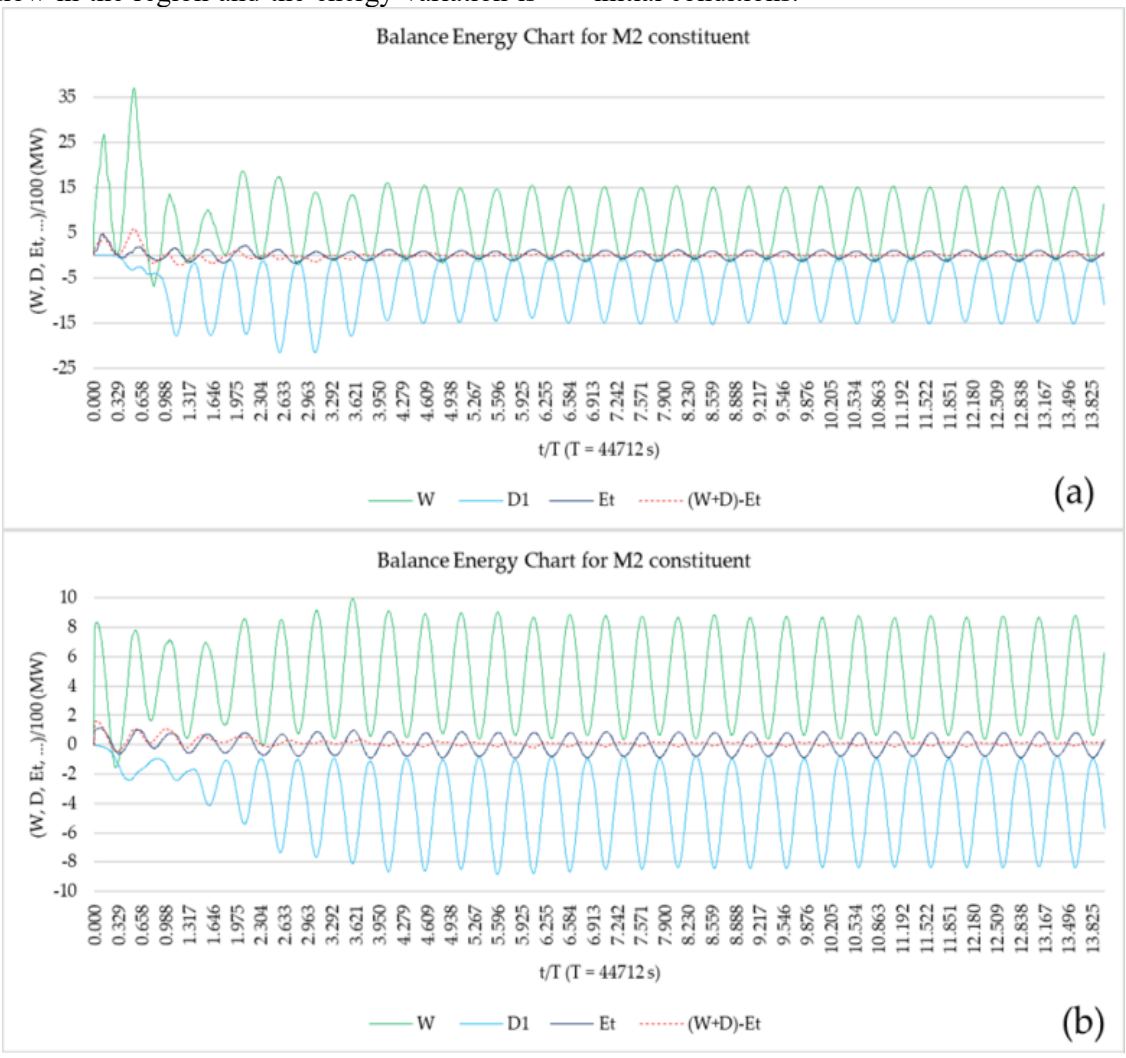

Fig.7 Balance energy chart of the Gulf of Tonkin (a) and that of the Gulf of Thailand (b)

3.3. The Harmonic Constants and Tidal Ellipses of the Tidal Constituents K_1, O_1, M_2, and S_2

The harmonic constant and the residual tidal ellipse maps were constructed from the amplitude and phase simulation results of the four main tidal constituents: K_1, O_1, M_2, S_2 (from the 5th period onwards). At the beginning of the periods (1st – 5th), the harmonic constituent oscillations are unstable.

For tidal constituent K_1, the amplitude simulations in the Gulf of Tonkin (0.2 – 0.8m) are larger than that of the Gulf of Thailand, about 0.2m (Fig. 8a). From Da Nang's position to Ca Mau Cape, the amplitude values reach a little gap of 0.2 – 0.4m while the tidal phase fluctuates from 0 degrees (Ca Mau Cape) to 340 degrees (Da Nang, Vietnam) (Fig. 8a). An amphidromous is recorded in the Gulf of Thailand (Fig. 8a). The residual tidal ellipses of the constituent prevail in the Gulf of Tonkin and Gulf of Thailand, which are a small residual tidal ellipse in the coastal of Vietnam (from Da Nang position to Ca Mau Cape) (Fig. 8b).

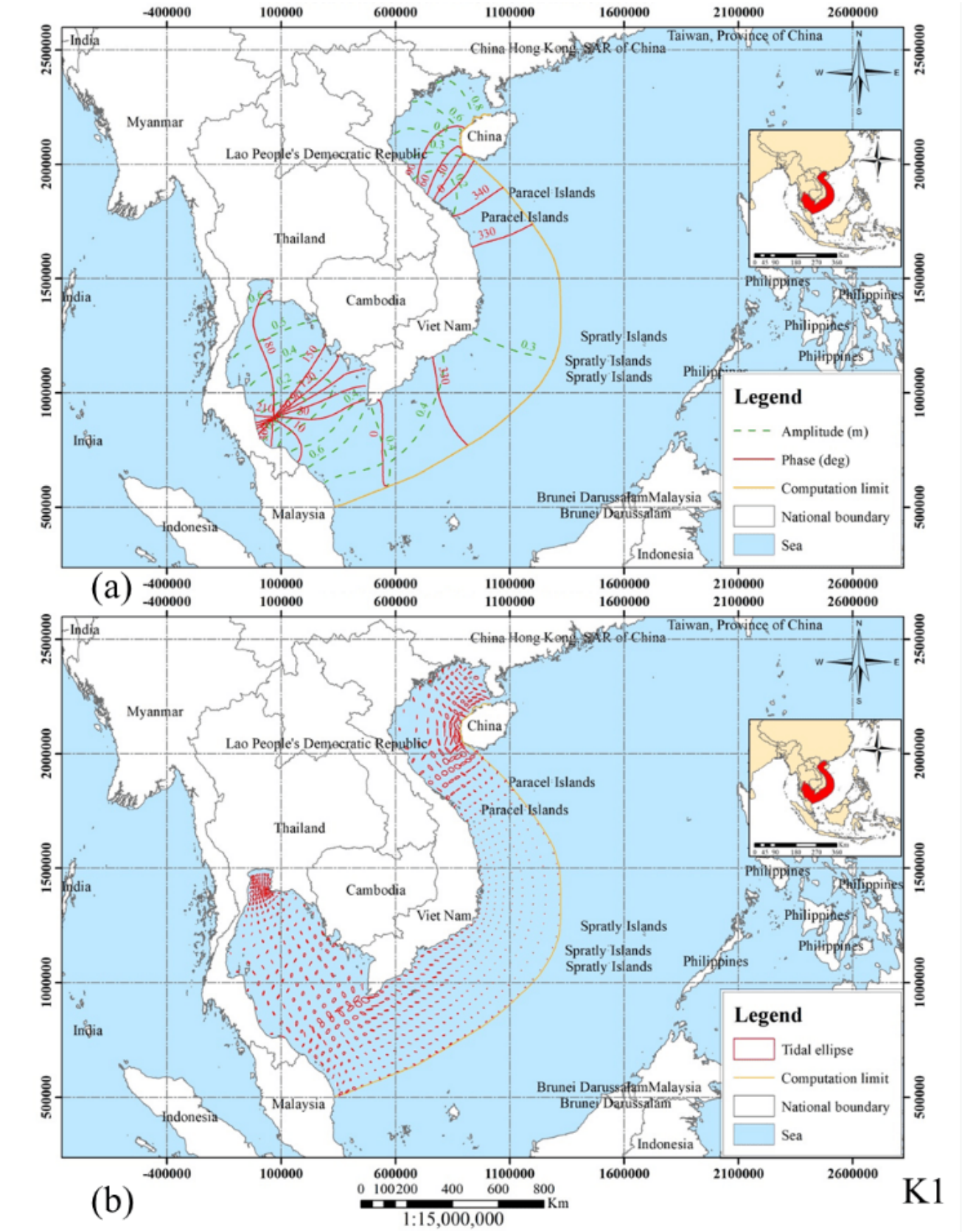

Fig.8 Harmonic constants (a) and the residual tidal ellipses (b) maps of K_1 constituent

For tidal constituent O_1, the tendency oscillation is similar to tidal constituent K_1. The tidal ellipses prevail in the Gulf of Tonkin and Gulf of Thailand, a small tidal residual ellipse in the coastal of Vietnam (from Da Nang position to Ca Mau Cape) (Fig. 9b). The highest tidal amplitude in the Gulf of Tonkin is 0.8m, double that in the Gulf of Thailand (Fig. 9a). The 0.2 – 0.3 are recorded from Da Nang position to Ca Mau Cape (Fig. 9a).

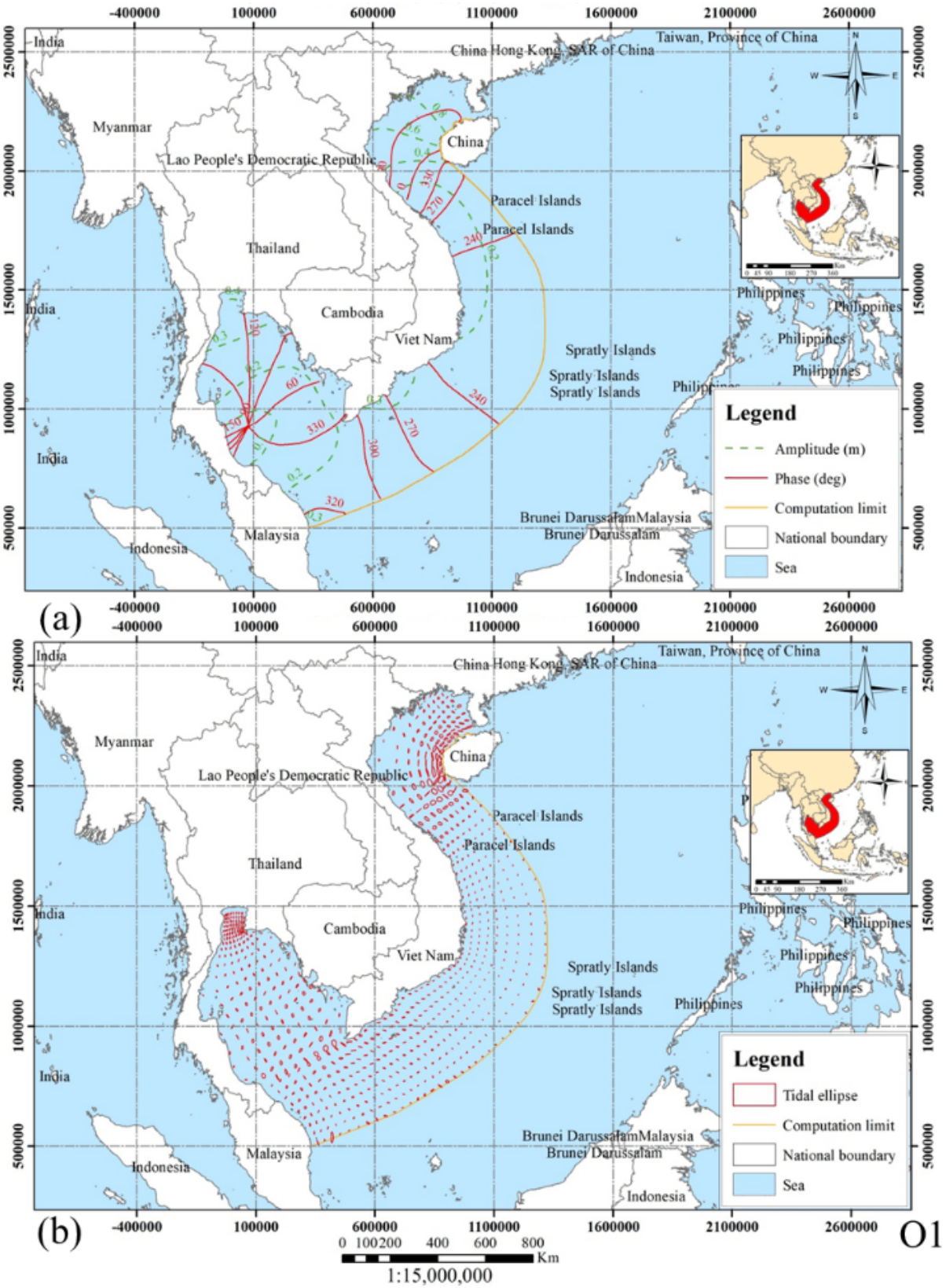

Fig.9 Harmonic constants (a) and the residual tidal ellipses (b) maps of O_1 constituent

For tidal constituent M_2, from Vung Tau to Ca Mau Cape, which semi-diurnal prevail, the tidal ellipses are the largest in the whole domain (Fig. 10b). There is an amphidromic point in the Gulf of Tonkin and two amphidromic points in the Gulf of Thailand (Fig. 10a). The highest tidal amplitude in the Gulf of Thailand is 0.4m, larger than that of Tonkin, a gap of 0.1m. From Da Nang's position to Ca Mau Cape, the tidal amplitudes increase when flowing to the coast, from 0.15 – 0.85m (Fig. 10a).

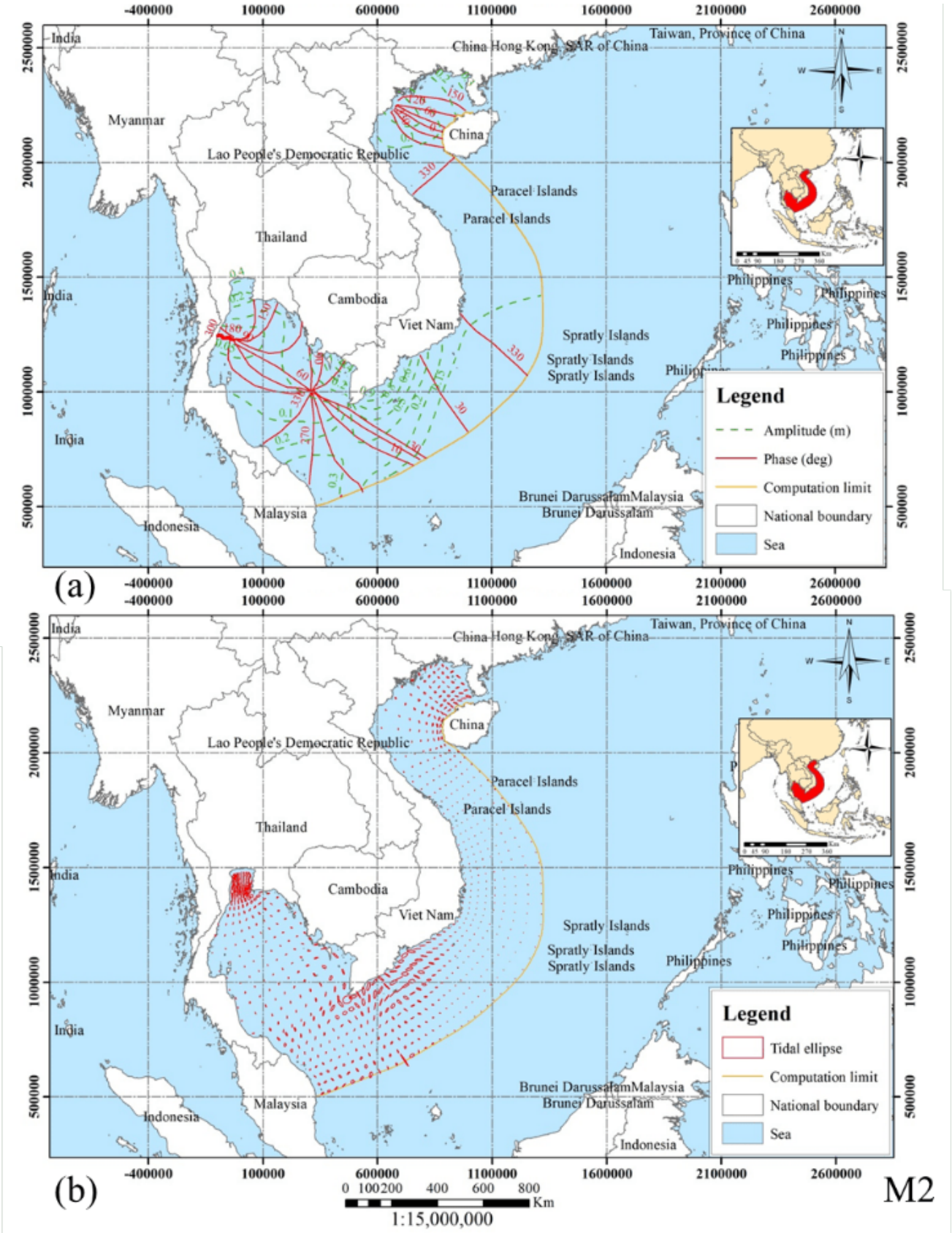

Fig.10 Harmonic constants (a) and the residual tidal ellipses (b) maps of M_2 constituent

For tidal constituent S_2, the tendency oscillation is similar to tidal constituent M_2. Two amphidromic points are also recorded in the Gulf of Thailand (Fig. 11a). The tidal amplitude from Vung Tau to Ca Mau cape reaches a gap of 0.1 - 0.3m (Fig. 11a). The amplitude value is little changed from Nha Trang to the Gulf of Tonkin, about 0.1m which is 0.3m in the Gulf of Thailand (Fig. 11a).

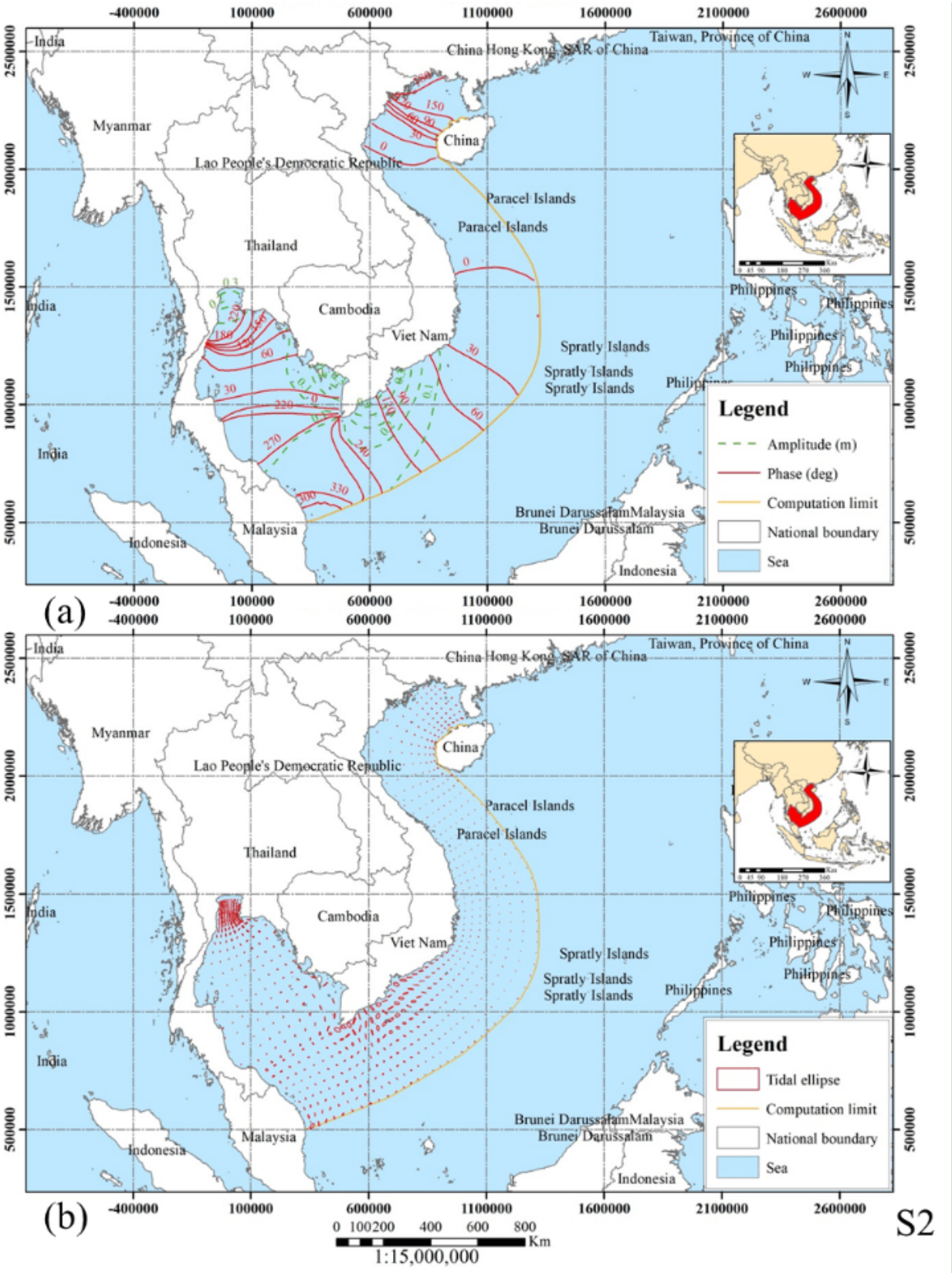

Fig.11 Harmonic constants (a) and the residual tidal ellipses (b) maps of K_2 constituent

4. Conclusion

This study uses a mathematical model in the curvilinear coordinate systems to study the tidal constitutes characteristics in the near-shore area where the friction bed coefficients change the water depth. The hydraulic model with the two-dimensional orthogonal curvilinear grid can increase the accuracy of the results at the domain boundary. In mathematical modeling, one of the difficulties encountered in solving geophysical problems is a coastal zone with complex topography. The widely used method of solving is to divide the coastal area into small segments, which are

parallel to the perpendicular coordinate axes (x, y). The disadvantage of this method is that the solution is much wrong in the coastal area. The curvilinear coordinate systems model will optimize the results for the near-shore area because the velocity field is calculated on a curved grid. Regarding mapping the harmonic constant of K_1, O_1, M_2, and S_2 tidal constituents and tidal ellipses in the near-shore East Sea area, Vietnam is the primary data for understanding the mechanisms causing the movement of the sediments. Moreover, that needs to be studied for future exploitation of clean energy.

The coastal area of Vietnam has potential tidal energy; the largest energy is the tidal constituent O_1, followed by the tidal constituents K_1, M_2, and S_2. The oscillation of the total energy (W) and loss of energy caused by bottom friction (D_1) has an opposite phase. In contrast, the total energy oscillates in phase with variation in energy in the domain (E_t). The energy balance oscillation in the variable region around axis '0' represents the energy balance in the region. The homogeneity of the oscillation of the energy inflow in the region and the energy variation is substantial for all four constituents, and the energy loss because friction is virtually small.

Tidal ellipses of the residual tidal constituent K_1 and O_1 are large in the Gulf of Tonkin and the Gulf of Thailand. Meanwhile, residual tidal constituent M_2 and S_2 are large in the southeast of Vietnam coastal. Although the tidal ellipses from the measurements for the near-shore area have not yet been taken to compare with the simulated results, the mathematical model results are similar to previous studies' results in the region.

References

[1] ABUBAKAR A. G., MAHMUD M. R., TANG K. K. W., HUSSAINI A., and YUSUF M. N. A review of modelling approaches on tidal analysis and prediction. *International Archives of the Photogrammetry, Remote Sensing Spatial Information Sciences*, 2019, XLII-4(W16), 23-34. https://doi.org/10.5194/isprs-archives-XLII-4-W16-23-2019

[2] LI S., LIU L., CAI S., and WANG, G. Tidal harmonic analysis and prediction with least-squares estimation and inaction method. *Estuarine, Coastal Shelf Science*, 2019, 220, 196-208. https://doi.org/10.1016/j.ecss.2019.02.047

[3] SARKAR D., OSBORNE M. A., and ADCOCK T. A. J. O. E. Prediction of tidal currents using Bayesian machine learning. *Ocean Engineering*, 2018, 158, 221-231. https://doi.org/10.1016/j.oceaneng.2018.03.007

[4] ABUBAKAR A., MAHMUD M., TANG K., and HUSAAINI A. The Determination of Tidal Constituents using Wavelet Base Harmonic at The Strait of Malacca. Proceedings of the the IOP Conference Series: Earth and Environmental Science, 2021. https://iopscience.iop.org/article/10.1088/1755-1315/731/1/012001/pdf

[5] MATHUR M., CARTER G. S., and PEACOCK T. Internal tide generation using green function analysis: to WKB or not to WKB? *Journal of Physical Oceanography*, 2016, 46(7), 2157-2168. https://doi.org/10.1175/JPO-D-15-0145.1

[6] NAGAR A., BERNUZZI S., DEL POZZO W., RIEMENSCHNEIDER G., AKCAY S., CARULLO G., FLEIG P., BABAK S., TSANG K. W., COLLEONI M., MESSINA F., PRATTEN G., RADICE D., RETTEGNO P., AGATHOS M., FAUCHON-JONES E., HANNAM M., HUSA S., DIETRICH T., CERDÁ-DURAN P., FONT J. A., PANNARALE F., SCHMIDT P., and DAMOUR T. Time-domain effective-one-body gravitational waveforms for coalescing compact binaries with nonprecessing spins, tides, and self-spin effects. *Physical Review D*, 2018, 98(10), 104052. https://doi.org/10.1103/PhysRevD.98.104052

[7] SUK H. Semi-analytical solution of land-derived solute transport under tidal fluctuation in a confined aquifer. *Journal of Hydrology*, 2017, 554, 517-531. https://doi.org/10.1016/j.jhydrol.2017.09.033

[8] POLLMANN F., NYCANDER J., EDEN C., and OLBERS D. Resolving the horizontal direction of internal tide generation. *Journal of Fluid Mechanics*, 2019, 864, 381-407. https://doi.org/10.1017/jfm.2019.9

[9] LE T. T., PHUNG D. H., and TRAN V. C. Numerical simulation of tidal flow in Danang Bay Based on non-hydrostatic shallow water equations. *Pacific Journal of Mathematics for Industry*, 2016, 8(1), 1-10. https://doi.org/10.1186/s40736-015-0020-6

[10] TANG J., LYU Y., SHEN Y., ZHANG M., and SU M. Numerical study on influences of breakwater layout on coastal waves, wave-induced currents, sediment transport and beach morphological evolution. *Ocean Engineering*, 2017, 141, 375-387. https://doi.org/10.1016/j.oceaneng.2017.06.042

[11] GAWEHN M., VAN DONGEREN A., DE VRIES S., SWINKELS C., HOEKSTRA R., and AARNINKHOF S., and FRIEDMAN J. The application of a radar-based depth inversion method to monitor near-shore nourishments on an open sandy coast and an ebb-tidal delta. *Coastal Engineering*, 2020, 159, 103716. https://doi.org/10.1016/j.coastaleng.2020.103716

[12] CAI S., LIU L., and WANG G. Short-term tidal level prediction using normal time-frequency transform. *Ocean Engineering,* 2018, 156, 489-499. https://doi.org/10.1016/j.oceaneng.2018.03.021

[13] YOUSEFI K., & VERON F. Boundary layer formulations in orthogonal curvilinear coordinates for flow over wind-generated surface waves. *Journal of Fluid Mechanics*, 2020, 888. https://doi.org/10.1017/jfm.2020.32

[14] MEDVEDEV I. P. Tides in the Black Sea: observations and numerical modelling. *Pure Applied Geophysics*, 2018, 175(6), 1951-1969. https://doi.org/10.1007/s00024-018-1878-x

[15] COLLINS D. S., AVDIS A., ALLISON P. A., JOHNSON H. D., HILL J., PIGGOTT M. D., HASSAN M. H. A., and DAMIT A. R. Tidal dynamics and mangrove carbon sequestration during the Oligo–Miocene in the South China Sea. *Nature communications,* 2017, 8(1), 1-12. https://doi.org/10.1038/ncomms15698

[16] WANG X., LIU Z., and PENG S. Impact of tidal mixing on water mass transformation and circulation in the

South China Sea. *Journal of Physical Oceanography*, 2017, 47(2), 419-432. https://doi.org/10.1175/JPO-D-16-0171.1
[17] DING Y., BAO X., YAO Z., ZHANG C., WAN K., BAO M., LI R., and SHI M. A modeling study of the characteristics and mechanism of the westward coastal current during summer in the northwestern South China Sea. *Ocean Science Journal*, 2017, 52(1), 11-30. https://doi.org/10.1007/s12601-017-0011-x
[18] DEVLIN A. T., JAY D. A., TALKE S. A., ZARON E. D., PAN J., and LIN, H. Coupling of sea level and tidal range changes, with implications for future water levels. *Scientific reports*, 2017, 7(1), 1-12. https://doi.org/10.1038/s41598-017-17056-z
[19] ANWAR K., HADITIAR Y., IKHWAN M., WAFDAN R., SETIAWAN I., MUCHLISIN Z., and RIZAL S. Numerical study of M2 tide on the Gulf of Thailand. Proceedings of the IOP Conference Series: Earth and Environmental Science, 2019. https://iopscience.iop.org/article/10.1088/1755-1315/348/1/012065/pdf
[20] GAO J., ZHU D., WU G., HU B., and HUANG H. Tidal and tidal current characteristics in the Guangxi Gulf of Tonkin, South China Sea. *Ocean Dynamics*, 2019, 69(9), 1037-1051. https://doi.org/10.1007/s10236-019-01294-y
[21] WEI Z., FANG G., SUSANTO R. D., ADI T. R., FAN B., SETIAWAN A., LI S., WANG Y., and GAO X. Tidal elevation, current, and energy flux in the area between the South China Sea and Java Sea. *Ocean Science*, 2016, 12(2), 517-531. https://doi.org/10.5194/os-12-517-2016
[22] FANG G., KWOK Y.-K., YU K., and ZHU Y. Numerical simulation of principal tidal constituents in the South China Sea, Gulf of Tonkin and Gulf of Thailand. *Continental Shelf Research*, 1999, 19(7), 845-869. https://doi.org/10.1016/S0278-4343(99)00002-3
[23] LI B.-D., ZHANG X.-H., TANG H.-S., and TSUBAKI R. Influence of deflection angles on flow behaviours in open-channel bends. *Journal of Mountain Science*, 2018, 15(10), 2292-2306. https://doi.org/10.1007/s11629-018-4848-y
[24] THI KIM T., HUONG N. T. M., HUY N. D. Q., TAI P. A., HONG S., QUAN T. M., BAY N. T., JEONG W.-K., and PHUNG N. K. Assessment of the Impact of Sand Mining on Bottom Morphology in the Mekong River in An Giang Province, Vietnam, Using a Hydro-Morphological Model with GPU Computing. *Water,* 2020, 12(10), 2912. https://doi.org/10.3390/w12102912

参考文:

[1] ABUBAKAR A. G., MAHMUD M. R., TANG K. K. W., HUSSAINI A., 和 YUSUF M. N. 潮汐分析和预测建模方法综述。国际摄影测量档案、遥感空间信息科学, 2019, XLII-4(W16), 23-34. https://doi.org/10.5194/isprs-archives-XLII-4-W16-23-2019
[2] LI S., LIU L., CAI S., 和 WANG, G. 潮汐谐波分析和预测与最小二乘估计和不作为方法。河口，海岸架科学, 2019, 220, 196-208. https://doi.org/10.1016/j.ecss.2019.02.047
[3] SARKAR D., OSBORNE M. A., 和 ADCOCK T. A. J. O. E. 使用贝叶斯机器学习预测潮流。海洋工程, 2018, 158, 221-231. https://doi.org/10.1016/j.oceaneng.2018.03.007
[4] ABUBAKAR A., MAHMUD M., TANG K., 和 HUSAAINI A. 用小波基谐波测定马六甲海峡的潮汐成分。物理研究所论文集系列：地球与环境科学, 2021. https://iopscience.iop.org/article/10.1088/1755-1315/731/1/012001/pdf
[5] MATHUR M., CARTER G. S., 和 PEACOCK T. 内潮代用绿色函数分析：去温策尔-克莱默斯-布里渊还是不去温策尔-克莱默斯-布里渊？物理海洋学杂志, 2016, 46(7), 2157-2168. https://doi.org/10.1175/JPO-D-15-0145.1
[6] NAGAR A., BERNUZZI S., DEL POZZO W., RIEMENSCHNEIDER G., AKCAY S., CARULLO G., FLEIG P., BABAK S., TSANG K. W., COLLEONI M., MESSINA F., PRATTEN G., RADICE D., RETTEGNO P., AGATHOS M., FAUCHON-JONES E., HANNAM M., HUSA S., DIETRICH T., CERDÁ-DURAN P., FONT J. A., PANNARALE F., SCHMIDT P., 和 DAMOUR T. 用于合并具有非进动自旋、潮汐和自旋效应的致密双星的时域有效单体引力波形。物理审查 D, 2018, 98(10), 104052. https://doi.org/10.1103/PhysRevD.98.104052
[7] SUK H. 承压含水层潮汐波动下陆源溶质运移半解析解。水文杂志, 2017, 554, 517-531. https://doi.org/10.1016/j.jhydrol.2017.09.033
[8] POLLMANN F., NYCANDER J., EDEN C., 和 OLBERS D. 解决内部潮汐产生的水平方向。流体力学杂志, 2019, 864, 381-407. https://doi.org/10.1017/jfm.2019.9
[9] LE T. T., PHUNG D. H., 和 TRAN V. C. 基于非静水浅水方程的岘港潮汐流数值模拟。太平洋工业数学杂志, 2016, 8(1), 1-10. https://doi.org/10.1186/s40736-015-0020-6
[10] TANG J., LYU Y., SHEN Y., ZHANG M., 和 SU M. 防波堤布局对海岸波浪、波浪诱导流、泥沙输送和海滩形态演化影响的数值研究。海洋工程, 2017, 141, 375-387. https://doi.org/10.1016/j.oceaneng.2017.06.042
[11] GAWEHN M., VAN DONGEREN A., DE VRIES S., SWINKELS C., HOEKSTRA R., 和 AARNINKHOF S., and FRIEDMAN J. 应用基于雷达的深度反演方法监测开阔沙质海岸和落潮三角洲的近岸营养物。海岸工程, 2020, 159, 103716. https://doi.org/10.1016/j.coastaleng.2020.103716
[12] CAI S., LIU L., 和 WANG G. 使用正常时频变换的短期潮位预测。海洋工程, 2018, 156, 489-499. https://doi.org/10.1016/j.oceaneng.2018.03.021
[13] YOUSEFI K., 和 VERON F. 风生表面波上流动的正交曲线坐标中的边界层公式。流体力学杂志, 2020, 888. https://doi.org/10.1017/jfm.2020.32
[14] MEDVEDEV I. P. 黑海潮汐：观测和数值模拟。纯应用地球物理学, 2018, 175(6), 1951-1969. https://doi.org/10.1007/s00024-018-1878-x

[15] COLLINS D. S., AVDIS A., ALLISON P. A., JOHNSON H. D., HILL J., PIGGOTT M. D., HASSAN M. H. A., 和 DAMIT A. R. 南海渐新世—中新世潮汐动力学与红树林固碳 [J]. 自然通讯, 2017, 8(1), 1-12. https://doi.org/10.1038/ncomms15698

[16] WANG X., LIU Z., 和 PENG S. 潮汐混合对南海水体转换和环流的影响。物理海洋学杂志, 2017, 47(2), 419-432. https://doi.org/10.1175/JPO-D-16-0171.1

[17] DING Y., BAO X., YAO Z., ZHANG C., WAN K., BAO M., LI R., 和 SHI M. 南海西北部夏季西向沿岸流特征及机制模拟研究.海洋科学杂志, 2017, 52(1), 11-30. https://doi.org/10.1007/s12601-017-0011-x

[18] DEVLIN A. T., JAY D. A., TALKE S. A., ZARON E. D., PAN J., 和 LIN, H. 海平面和潮差变化的耦合，对未来水位产生影响。科学报告, 2017, 7(1), 1-12. https://doi.org/10.1038/s41598-017-17056-z

[19] ANWAR K., HADITIAR Y., IKHWAN M., WAFDAN R., SETIAWAN I., MUCHLISIN Z., 和 RIZAL S. 泰国湾 M2 潮数值研究。物理研究所论文集系列：地球与环境科学, 2019. https://iopscience.iop.org/article/10.1088/1755-1315/348/1/012065/pdf

[20] GAO J., ZHU D., WU G., HU B., 和 HUANG H. 南海广西北部湾潮汐及潮流特征.海洋动力学, 2019, 69(9), 1037-1051. https://doi.org/10.1007/s10236-019-01294-y

[21] WEI Z., FANG G., SUSANTO R. D., ADI T. R., FAN B., SETIAWAN A., LI S., WANG Y., 和 GAO X. 南海和爪哇海之间海域的潮汐高程、洋流和能量通量。海洋科学, 2016, 12(2), 517-531. https://doi.org/10.5194/os-12-517-2016

[22] FANG G., KWOK Y.-K., YU K., 和 ZHU Y. 南海、东京湾和泰国湾主要潮汐成分的数值模拟。大陆架研究, 1999, 19(7), 845-869. https://doi.org/10.1016/S0278-4343(99)00002-3

[23] LI B.-D., ZHANG X.-H., TANG H.-S., 和 TSUBAKI R. 偏转角对明渠弯道流动行为的影响。山地科学杂志, 2018, 15(10), 2292-2306. https://doi.org/10.1007/s11629-018-4848-y

[24] THI KIM T., HUONG N. T. M., HUY N. D. Q., TAI P. A., HONG S., QUAN T. M., BAY N. T., JEONG W.-K., 和 PHUNG N. K. 使用 图形处理器 计算的水文形态模型评估采砂对越南安江省湄公河底部形态的影响。水, 2020, 12(10), 2912. https://doi.org/10.3390/w12102912